



The M7 2016 Kumamoto, Japan, Earthquake: 3D coseismic deformation from differential topography

Scott, Chelsea (1), Arrowsmith, Ramon (2), Lajoie, Lia (3), Nissen, Edwin (4), Maruyama, Tadashi (5), Chiba, Tatsuro (6)

- (1) School of Earth and Space Exploration, Arizona State University, Tempe, Arizona, USA. cpsott1@asu.edu;
- (2) Arizona State University, Arizona, USA;
- (3) Colorado School of Mines, Colorado, USA;
- (4) University of Victoria, Victoria, Canada;
- (5) Geological Survey of Japan, Japan;
- (6) Asia Air Survey Co., Japan.

Abstract: The April 2016 Kumamoto earthquake sequence ruptured the Hinagu and Futagawa faults on the Kyushu Island of southwestern Japan. Our work concentrates on the M7 mainshock, which ruptured 30km of fault length with an oblique strike-slip mechanism and surface slip exceeding 2m. We present 3D near-fault displacements determined from the differencing of high-resolution topography acquired before and after the mainshock. To examine the mechanical properties of the shallow fault zone, we jointly invert the near-field lidar and InSAR displacements to solve for distributed fault slip. Our earthquake source inversion suggests that fault slip is depleted in the upper 100m of the crust relative to 500m depth. A comparison to published field measurements suggests additional slip depletion near the surface. Differential topography and InSAR data resolve slip throughout the seismogenic zone and are indicative of the physical processes that control the transmission of slip from the shallow crust to the surface.

Key words: Earthquake deformation, differential topography, InSAR

INTRODUCTION

Observations of coseismic deformation place valuable constraints on the location of active faults, the distribution of slip in the seismogenic zone, and the mechanical properties of the fault volume. Near-fault displacements from differential topography bridge the observational gap between on-fault field measurements of offset and InSAR displacements that determine the far-field deformation but often lose coherence near the fault. We use near-field displacements to study the behavior of the shallow fault zone and the localization of fault slip. Multiple previous studies including Rockwell *et al.* [2002], Nissen *et al.* [2014] and Milliner *et al.* [2015] show significant distributed surface deformation within ~100 m of the fault. To quantify this near-surface depletion of shallow fault slip, we construct a distributed slip model from near-field differential lidar topography and far-field InSAR displacements. Our results show that differential topography and InSAR datasets place

constraints on fault slip in the upper portion of the seismogenic zone and contribute to a deeper understanding of the mechanical properties of the fault.

The well-documented near-fault surface displacements produced by the April 16 2016 M7 Kumamoto, Japan, earthquake offer unusual insight into the behavior of the shallow fault zone. We present 3D near-fault displacement fields constrained from the differencing of high-resolution topography acquired before and after the mainshock. We examine two approaches for quantifying depth-dependent variations in fault slip. First, we calculate differential displacements at increasing apertures across the fault. Second, we solve for fault geometry and distributed slip in a joint-inversion of the near-field lidar and far-field InSAR displacements. Both approaches suggest that fault slip is depleted in the upper 100 m of the crust relative to 500 m depth. A comparison of the modeled slip to published field

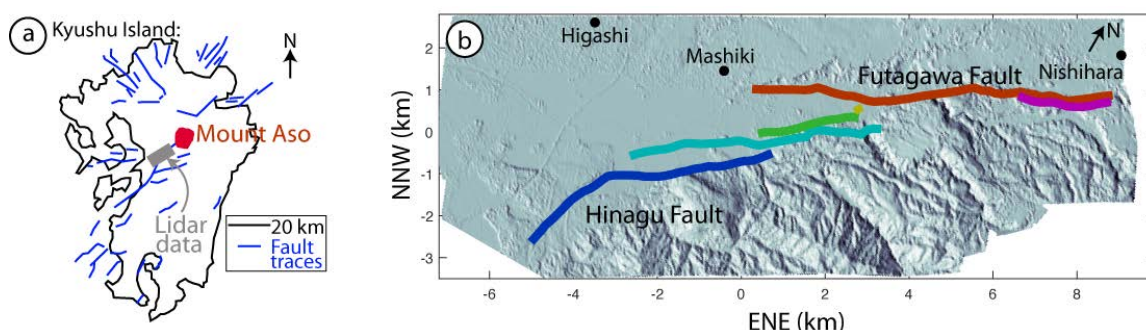


Figure 1: (a) Kyushu island of southwestern Japan. Grey box: location of lidar datasets acquired before and after the mainshock. Blue lines: faults from the Active fault database of Japan [AIST, 2017]. (b) Shaded relief map produced from the lidar elevations. Colored lines indicate fault segments that ruptured in the M7 Kumamoto earthquake, and the color corresponds to the slip profile in Figure 3.



INQUA Focus Group Earthquake Geology and Seismic Hazards



paleoseismicity.org

measurements suggests an additional depletion of slip from a 100 m depth to the surface. The high surface strains of 1 to 4% in the ~100 m surrounding the fault suggest that the elastic strength of rocks is exceeded in the fault volume and that the depleted fault slip is accommodated by off-fault folding and fracturing at a finer scale than our analysis.

METHODS

Lidar data: Motivated by the M_w 6.2 foreshock on 14 April 2016, the Asia Air Survey Company acquired the pre-mainshock lidar dataset on 15 April 2016 at the location shown in Figure 1. The post-mainshock dataset was acquired on 23 April 2016 with the same pilot, aircraft, and lidar instrument as the first dataset. The pre- and post-mainshock datasets have shot densities of 2.5 and 3.5 points/m², respectively.

3D deformation: We use a windowed implementation of the piecewise Iterative Closest Point algorithm [ICP; Besl and McKay, 1992; Chen and Medioni, 1992] to determine the 3D surface deformation field produced by the M7 Kumamoto earthquake shown in Figure 2. We calculate the deformation at a set of core points from the optimal

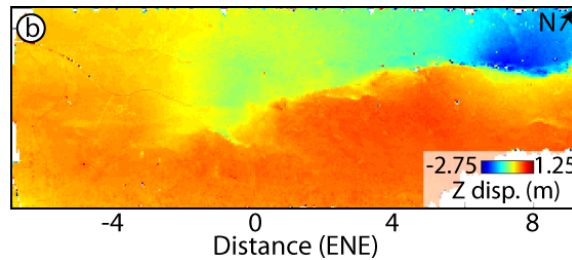
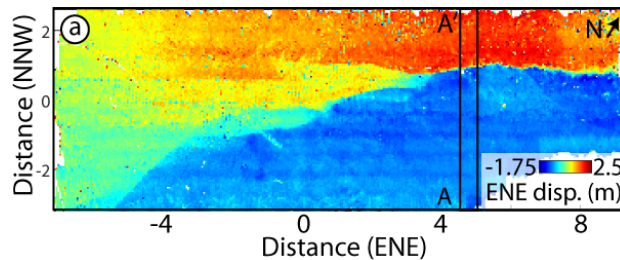


Figure 2: Iterative Closest Point (ICP) results showing (a) the east-northeast and (b) the vertical displacement fields for the 2016 M7 Kumamoto earthquake. The A-A' transect is shown in Figure 4.

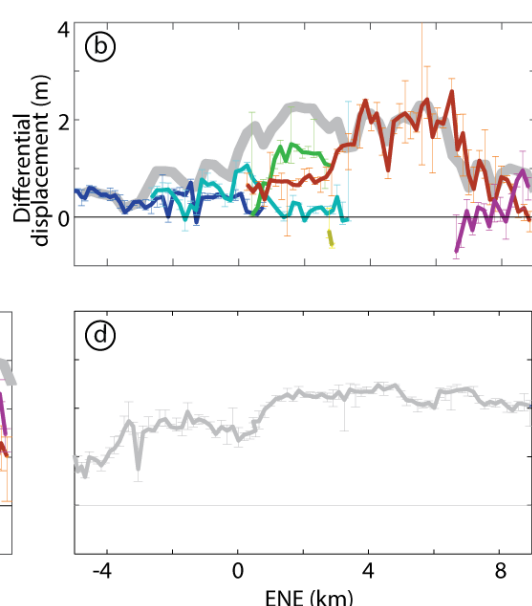
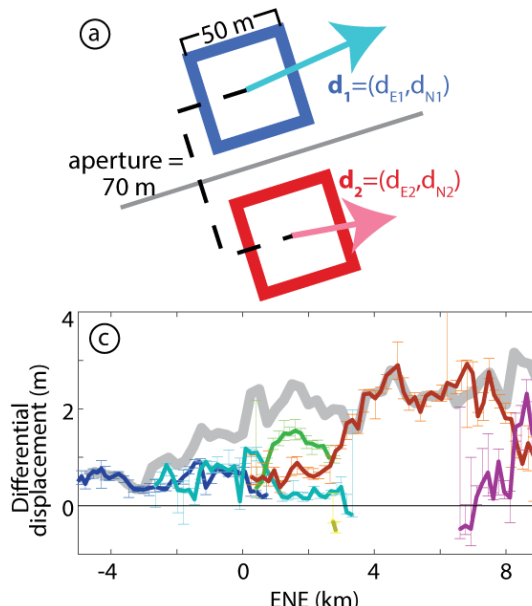


Figure 3: Right-lateral ICP differential displacements. (a) Schematic illustration showing the geometry of the differential displacement calculation over an aperture of 70 m. The grey line is the fault trace. The light blue and pink arrows show the displacement calculated from the pre- and post-earthquake point cloud data in the blue and red boxes, respectively. (b) Differential displacement calculated at an aperture of 70 m as illustrated in (a). The colored lines correspond to individual fault segments shown in Figure 1b. The thick grey line is the summed slip on all fault segments within a moving window. (c) Differential displacements calculated at an aperture of 200 m. (d) Differential displacements calculated at an aperture of 2000 m. This larger aperture calculation represents the summed displacement from all faults.

rotation and displacement required to align 50 m windowed subsets of the pre- and post- earthquake point cloud data. We implement the LIBICP software developed by Geiger *et al.* [2012]. The deformation of the pre-earthquake point cloud dataset (PC_{pre}) that produces the deformed point cloud ($PC_{deformed}^{pre}$) is,

$$PC_{pre}^{deformed} = \begin{pmatrix} 1 & -\gamma & \beta \\ \gamma & 1 & -\alpha \\ -\beta & \alpha & 1 \end{pmatrix} PC_{pre} + \begin{pmatrix} t_x \\ t_y \\ t_z \end{pmatrix}, \quad (1)$$

where α , β and λ , are rotations about the x, y and z axes, and t_x , t_y and t_z are translations in the x, y, and z directions. The solution is penalized for misalignments between $PC_{pre}^{deformed}$ and the post-earthquake point-cloud dataset.

We develop an approach for computing displacement uncertainty, and demonstrate that the performance of the ICP method depends on the local topographic roughness. Errors range from 10 cm over higher relief and forested areas to 25 cm over flatter agricultural lands.

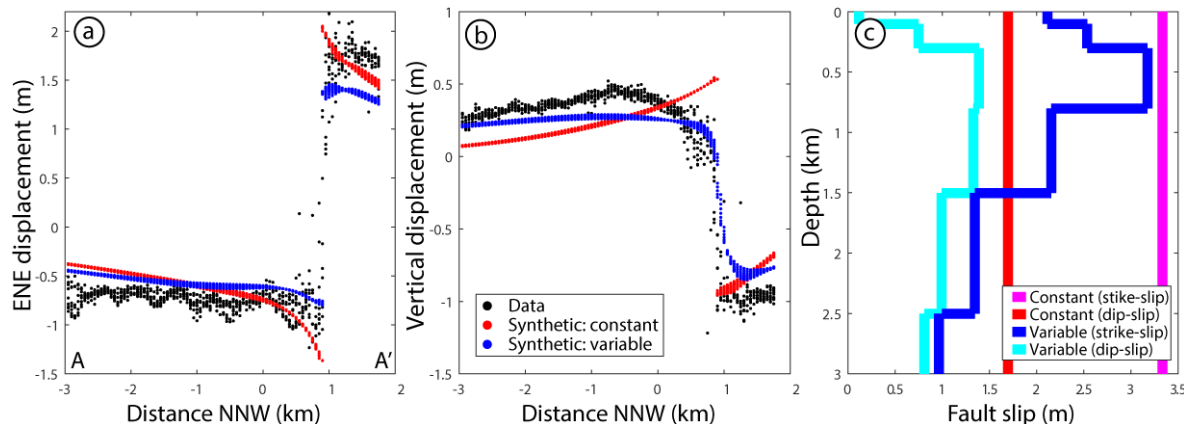


Figure 4: Earthquake source inversion results along the A-A' transect in Figure 2a. (a) ENE displacement showing ICP displacements (black), surface displacements produced by a fault model where slip is constant with depth (red) and varies with depth (blue). (b) Vertical displacement with the same colors as in (a). (c) Depth vs. fault slip: Strike-slip (pink) and dip-slip (red) profiles when slip is constant with depth. Strike-slip (blue) and dip-slip (light blue) when slip varies with depth. Slip continues to decrease with depth for the depth-dependent slip model.

Differential displacement: We calculate displacement discontinuities from ICP displacements at points that lie on opposite sides of the fault as a metric for fault slip as shown in Figure 3a. We align the ICP coordinate system with the fault trace shown in grey. We separate the center of the ICP boxes by the aperture of interest. For a 70 m aperture, the ICP boxes are placed 70 m apart

leaving a 10 m buffer between the edge of the ICP box and the fault trace. We calculate the right-lateral displacement (d_r) by projecting the difference in displacement across the fault along the fault strike:

$$d_r = ((d_{E1}, d_{N1}) - (d_{E2}, d_{N2})) \cdot \langle \text{fault strike} \rangle \quad (2)$$

where d_{E1} and d_{N1} are the east and north displacements, respectively, on the northern side of the fault, d_{E2} and d_{N2} are the displacements on the southern side of the fault, and $\langle \text{fault strike} \rangle$ is a unit vector oriented parallel to the local fault strike.

Joint lidar and InSAR earthquake source inversion: We conduct a joint inversion of our lidar displacements and the InSAR data from Jiang et al. [2017] to constrain along-strike and depth-dependent variations in fault slip (Figure 4). We solve for the fault geometry in 500 m segments to capture the sub-kilometer complexity in the fault rupture pattern. Fault slip does not vary with depth in our ‘depth-independent slip model.’ In the ‘depth-dependent slip model,’ we solve for distributed slip in fault patches whose dimension increases with depth according to the decreased resolving power of the data [Lohman and Simons, 2005; Barnhart and Lohman, 2010]. For both slip models, we allow the rake to vary spatially and impose smoothing and minimum norm constraints on the fault slip.

DISCUSSION

The 16 April 2016 Kumamoto earthquake propagated from its epicenter near the town of Higashi (Figure 1) to the NNE-striking Hinagua fault [Yagi et al., 2016]. The earthquake then ruptured the NE-striking Futagawa fault,

which hosted the dominant moment release. As shown in the ICP-derived displacement maps in Figure 2, the earthquake accommodated right-lateral and southeast-side-up motion. The Hinagu fault accommodated a maximum right-lateral fault slip of 0.5 m and negligible vertical slip. East of Mashiki, the earthquake ruptured a northern and southern strand of the Futagawa fault with right-lateral slip on the individual strands varying from 0.5–1.5 m and decimeter-scale vertical slip. When the two strands joined to a single strand, slip exceeded 2 m. The fault bifurcated to the ENE, and the fault stands accommodated 2 m of both right-lateral motion and subsidence distributed over 3 km.

We calculate differential displacement at apertures of 70 m, 200 m, and 2000 m as a measure of fault slip at increasing depths (Figure 3). The differential displacement calculated at an aperture of 70 m reaches a maximum of 2.25 m along the red segment of the Futagawa fault (Figure 1b). The summed displacement curve shows an roughly elliptical slip envelope beginning at the Hinagu fault that continues to grow as slip is transferred to the Futagawa fault. At the 200 m aperture, the differential displacement is equal to or exceeds the 70 m aperture displacement. At the 2000 m aperture, the differential displacement is smoother than at the narrower apertures, suggesting a dampening of the slip heterogeneity present closer to the fault. In the zone of fault bifurcation to the ENE, the differential displacement is 3 m at the 200 m aperture and decreases to 2.25 m at the 2000 m aperture. This suggests a concentration of off-fault deformation at a distance of 100 m to 1 km from the fault, likely indicating elevated fault slip at similar depths.

We compare the lidar and InSAR-derived earthquake source inversion results for the depth-independent and depth-dependent slip models along the segment of the Futagawa fault in the A-A' transect. The ENE lidar displacements show a 2.5 m displacement step along the fault (Figure 4a). The depth-independent slip model does not replicate the concavity of the displacement signal and overpredicts the fault offset by 1 m. The depth-dependent slip model replicates the concavity, yet underpredicts slip



INQUA Focus Group Earthquake Geology and Seismic Hazards



paleoseismicity.org

by 0.5 m. The vertical displacement (Figure 4b) shows an on-fault offset of 1 m and additional distributed displacement over 1 km of the footwall. The depth-dependent slip model reproduces the concavity of the displacement signal yet underpredicts the surface slip. We conclude that the depth-dependent slip model replicates both the shape and the magnitude of the displacement signal better than the depth-independent model. The depth-dependent slip model suggests a maximum right-lateral slip of 3 m at 0.4 to 0.8 km depth (Figure 4c) that decays to 2.5 m at 0.1 to 0.4 km depth and to 2 m at the surface. The dip-slip reaches a maximum value of 1.5 m from depths of 0.4 to 1.5 km and decays rapidly near the surface.

CONCLUSION

We use the ICP algorithm to calculate the near-fault 3D coseismic displacements for the 2016 Kumamoto earthquake from pre- and post-earthquake lidar datasets. The displacement field illustrates the development of the rupture and the distribution of both on- and off-fault deformation. We combine near-field lidar and far-field InSAR displacements to solve for distributed fault slip throughout the seismogenic zone. These results show a depletion of fault slip in the upper 100 m of the crust. The high surface strains of 1 to 4% in the ~100 m that surround the fault suggest the depleted fault slip is accommodated as off-fault deformation.

We use high-resolution topography to infer slip at the shallow depths that are commonly elusive to seismic and geodetic datasets. Our observation of depleted slip in the upper 100 m of the crust has implications for the frictional properties of the shallow crust and the interpretation of earthquake behavior from the paleoseismic and geomorphic records. As more earthquakes are observed with lidar data, the earthquake community will be able to better understand the physics of shallow faults and the hazards posed by crustal faults.

Acknowledgements: C. Scott is supported by the US NSF Postdoctoral Fellowship 1625221.

REFERENCES

- Barnhart, W. D., and R. B. Lohman (2010), Automated fault model discretization for inversions for coseismic slip distributions, *J. Geophys. Res.*, 115(B10), doi:10.1029/2010JB007545.
- Besl, P. J., and N. D. McKay (1992), A method for registration of 3-D shapes, *IEEE Trans. Pattern Anal. Mach. Intell.*, 14(2), 239–256, doi:10.1109/34.121791.
- Chen, Y., and G. Medioni (1992), Object modelling by registration of multiple range images, *Image Vis. Comput.*, 10(3), 145–155, doi:10.1016/0262-8856(92)90066-C.
- Geiger, A., P. Lenz, and R. Urtasun (2012), Are we ready for autonomous driving? The KITTI vision benchmark suite, pp. 3354–3361, IEEE.
- Jiang, H., G. Feng, T. Wang, and R. Bürgmann (2017), Toward full exploitation of coherent and incoherent information in Sentinel-1 TOPS data for retrieving surface displacement: Application to the 2016 Kumamoto (Japan) earthquake, *Geophys. Res. Lett.*, doi:10.1002/2016GL072253.
- Lohman, R. B., and M. Simons (2005), Some thoughts on the use of InSAR data to constrain models of surface deformation: Noise structure and data downsampling, *Geochem. Geophys. Geosystems*, 6(1), doi:10.1029/2004GC000841.
- Milliner, C. W. D., J. F. Dolan, J. Hollingsworth, S. Leprince, F. Ayoub, and C. G. Sammis (2015), Quantifying near-field and off-fault deformation patterns of the 1992 M_w 7.3 Landers earthquake: Deformation of the Landers earthquake, *Geochem. Geophys. Geosystems*, 16(5), 1577–1598, doi:10.1002/2014GC005693.
- National Institute of Advanced Industrial Science and Technology (AIST; 2017), Active fault database of Japan.
- Nissen, E., T. Maruyama, J.R. Arrowsmith, J. R. Elliott, A. K. Krishnan, M. E. Oskin, and S. Saripalli (2014), Coseismic fault zone deformation revealed with differential lidar: Examples from Japanese □7 intraplate earthquakes, *Earth Planet. Sci. Lett.*, 405, 244–256, doi:10.1016/j.epsl.2014.08.031.
- Rockwell, T. K., S. Lindvall, T. Dawson, R. Langridge, W. Lettis, and Y. Klinger (2002), Lateral Offsets on Surveyed Cultural Features Resulting from the 1999 Izmit and Duzce Earthquakes, Turkey, *Bull. Seismol. Soc. Am.*, 92(1), 79–94, doi:10.1785/0120000809.
- Yagi, Y., R. Okuwaki, B. Enescu, A. Kasahara, A. Miyakawa, and M. Otsubo (2016), Rupture process of the 2016 Kumamoto earthquake in relation to the thermal structure around Aso volcano, *Earth Planets Space*, 68(1), doi:10.1186/s40623-016-0492-3.